Article

Effect of the Heterogeneity of Coal on Its Seepage Anisotropy: A Micro Conceptual Model

Xiuling Chen [1,2], Guanglei Cui [1,2,*], Jiaming Luo [1,2], Chunguang Wang [3,*] and Jian Zhang [4]

1 Key Laboratory of Ministry of Education on Safe Mining of Deep Metal Mines, School of Resources and Civil Engineering, Northeastern University, Shenyang 110819, China; 2401008@stu.neu.edu.cn (X.C.); 2371109@stu.neu.edu.cn (J.L.)
2 Key Laboratory of Liaoning Province on Deep Engineering and Intelligent Technology, Northeastern University, Shenyang 110819, China
3 State Key Laboratory of Mining Disaster Prevention and Control Co-Founded by Shandong Province and the Ministry of Science and Technology, Shandong University of Science and Technology, Qingdao 266590, China
4 College of Water Conservancy and Civil Engineering, Shandong Agricultural University, No.61 Daizong Street, Taian 271018, China; zhangj614@163.com
* Correspondence: cuiguanglei@mail.neu.edu.cn (G.C.); chunguangkuangda@126.com (C.W.)

Abstract: Coal is a typical dual-porosity structural material. The injection of CO_2 into coal seams has been shown to be an effective method for storing greenhouse gasses and extracting coal bed methane. In light of the theory of dual-porosity media, we investigate the impact of non-homogeneity on seepage anisotropy and examine the influence of CO_2 gas injection on the anisotropy of coal and the permeability of fractures. The results demonstrate that under constant pressure conditions, coal rock has the greatest permeability variation in the direction of face cleats and the smallest changes in the direction of vertical bedding. The more pronounced the heterogeneity, the more evident the change in permeability and the less pronounced the decreasing stage of permeability. Additionally, the larger the diffusion coefficient is, the less pronounced the permeability change. The change in permeability is inversely proportional to the size of the adsorption constant and directly proportional to the size of the fracture. As the matrix block size increases, the permeability also increases, whereas the decrease in permeability becomes less pronounced. The findings of this study offer a theoretical basis for further research into methods for enhancing the CO_2 sequestration rate.

Keywords: numerical simulation; permeability; storage of greenhouse gasses; dual-porosity media; fracture opening

1. Introduction

In light of the significant threat that global warming poses to Earth's living systems, stringent control of CO_2 emissions to reduce greenhouse gas output has emerged as a consensus among countries worldwide [1–3]. Considering economic development alongside carbon emissions, future carbon neutrality may increasingly depend on negative emission technologies such as carbon sequestration. Geological storage exemplifies a typical negative emission technology (see, for example, Figure 1a), providing potential for sustainable long-term CO_2 storage [4]. Common geological storage methods for CO_2 include depleted oil and gas reservoirs, saline aquifers, coal seams, and basalt formations. The adsorption capacity of coal for CO_2 is about twice that of CH_4, which is a natural adsorbent for CO_2 [5]. In addition, the cost of coal seam CO_2 storage technology is low, facilitating the efficient recovery of coal bed methane [6]. Coal seam CO_2 sequestration not only reduces the atmospheric concentration of CO_2 but also helps reduce the emission of greenhouse gasses, which is in line with the national concept of green development [7]. Therefore, coal seam CO_2 sequestration is anticipated to become a primary method of carbon sequestration.
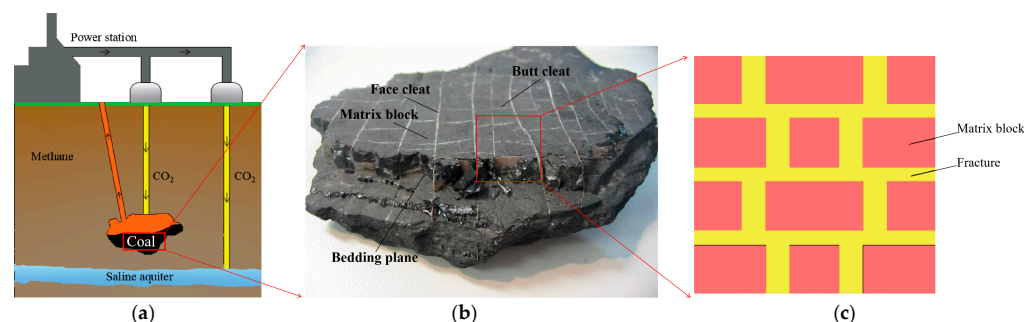
Figure 1. Schematic diagram of the coal structure. (**a**) Geological sequestration, (**b**) coal sample, and (**c**) one of the floor plans.

Coal rock is a solid, combustible, organic rock characterized by a complex structure formed through weathering, erosion, transport, and deposition of coal particles, carbonates, clays, and various minerals over extended periods. Numerous primary pores and fractures are present, with the fractures distributed in a crosswise manner, exhibiting distinct discontinuities and nonuniformities [8,9]. This characteristic is depicted in Figure 1b,c, indicating that coal rock can be classified an anisotropic porous medium [10]. The flow of fluids within rock formations and the mechanical properties of rocks are also anisotropic [11–13]. Coal represents a typical dual-porosity medium consisting of a matrix and fractures [14], as illustrated in Figure 1. With respect to mechanical properties [15], the mechanical behavior of anthracite under various loading conditions was investigated by Okubo et al. [16] using uniaxial compression and tensile tests. The results indicated that alignment of the loading direction with the bedding planes or fractures of coal rock could result in changes in mechanical properties, including compressive strength and tensile strength. Additionally, anisotropy was demonstrated. Li et al. [17] examined the effect of loading direction on the stability of coal sample splitting through Brazilian splitting experiments. The experimental results revealed that the destructive load is greater when the loading direction is perpendicular to the coal rock bedding planes and is lower when the loading direction is parallel to the coal rock bedding planes. The destructive load increases in a perpendicular loading direction relative to the coal bedding, whereas it decreases when aligned with the bedding. Comprehensive laboratory experiments and numerical simulations were conducted by Zhao et al. [18] to analyze the effect of bedding on the dynamic indirect tensile strength of coal. These findings indicate that the mechanical properties of coal display significant anisotropic characteristics, which are heavily influenced by the structural arrangement of the laminae. When the loading direction aligns with the bedding planes, a lower tensile strength is observed, increasing the likelihood of fracture propagation along the laminar surface. In contrast, with a perpendicular loading direction, a significant increase in tensile strength can be observed, resulting in more complex and irregular fracture propagation. In a subsequent study, Zhao et al. [19] assessed the influence of bedding inclination and loading rate on the fracture toughness of coal samples. The results demonstrated that the characteristics of fracture propagation in coal were significantly affected by bedding planes under impact loading, resulting in marked anisotropy.

With respect to permeability characteristics, Pomeroy et al. [20] identified a significant difference in permeability through water seepage tests conducted with confining pressures oriented parallel and perpendicular to bedding planes. This finding suggests that vertical mechanics influence the flow capacity in the horizontal direction and that the mechanical properties in the horizontal direction also affect the flow capacity in the vertical direction. The permeability in the parallel direction is a dozen times greater than that in the vertical direction, as demonstrated by Koenig and Stubbs in their investigation of permeability variations in several bedding coal samples [21]. Anisotropic permeability, resulting from the distinct development of bedding and cleat structures throughout the mechanical stress history, was noted by Gash et al. [22] The permeabilities of coal exhibit significant differences in 3D [23]. Yan et al. [24] utilized a self-developed permeability measurement system

to evaluate the permeability of coal under varying stress conditions. The drilling of coal cores revealed that the highest permeability occurred along the strike direction, whereas the lowest permeability occurred in the vertical direction, with an intermediate permeability occurring in the dip direction.

Permeability is a physical parameter that quantifies the ease of fluid flow within a rock and is not only dependent on pore topology but also significantly affected by rock structure and other structural characteristics. Numerous coal permeability models [11,25–35] have been developed to accurately forecast natural gas production from onsite wells and to interpret laboratory permeability data. Zhang et al. [25] introduced a general model linking permeability to porosity, accounting for pore changes due to effective stress and gas adsorption simultaneously. Building upon this model, Liu et al. [32] addressed the intrinsic interactions between the matrix and fracture. In subsequent research by Peng et al. [30], the concept of effective strain was introduced, incorporating local strain and global strain. More recently, several researchers have integrated both the gas slip effect and deformation caused by effective stress into shale permeability models. Wang et al. [28] presented a more complex permeability model that encompasses the effects of gas adsorption, effective stress compression, and gas slip. Liu et al. [33] proposed a permeability model incorporating internal expansion stress and considering matrix–fracture interactions during coal seam deformation, although it fails to account for permeability data under varying confining pressures.

The isotropic assumption underpins the current permeability model. Given that both the flow and mechanical properties of coal rock are significantly anisotropic, this approach introduces inaccuracies when characterizing variations in anisotropic permeability in coal [36]. Wang et al. [29] proposed a permeability model that incorporates both mechanical deformation and structural anisotropy. Additionally, another anisotropic permeability model [11] offers advantages by analyzing anisotropic permeability, considering both fracture structure and deformation characteristics, and treating the matrix and fractured coal as an equivalent elastic continuum. Yang et al. [26] considered coal as a transversely isotropic medium and accounted for the coupling effects of adsorption and effective stress in the permeability model. This model is employed during coal bed methane extraction to investigate gas transport behavior as well as the factors influencing permeability in three directions. Li et al. [35] investigated the impact of anisotropic adsorption deformation on coal permeability evolution.

The above studies show that the difference in the mechanical properties of the coal mass and matrix controls the variation in coal permeability, but few theoretical models have been conducted on these two factors. In this work, theoretical modeling and numerical simulation are employed to study the impact of fracture and matrix mechanical anisotropy on permeability evolution in various directions. In the second part of the study (illustrated in Figure 2a), coupled modeling was conducted, whereas in the third part (depicted in Figure 2b), modeling was performed. In the fourth part of the study (depicted in Figure 2c), a parametric analysis was carried out.
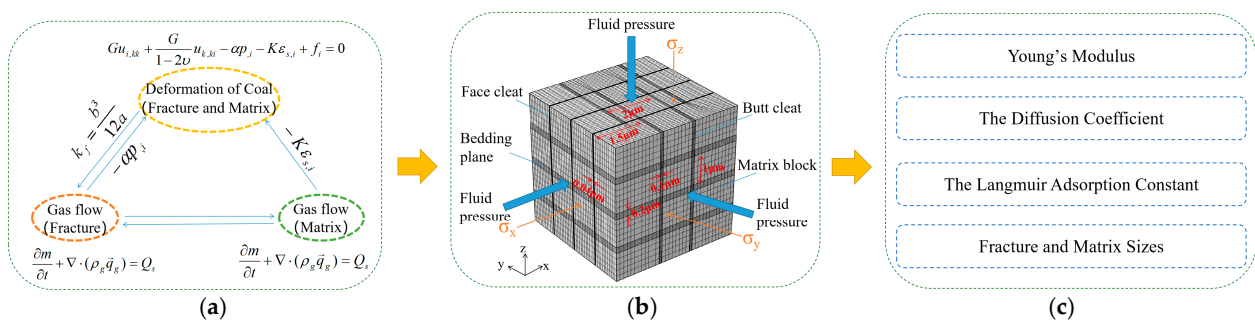

Figure 2. Geometry model and meshing. (**a**) Coupling relationship, (**b**) model validation, (**c**) parametric analysis.

2. Mathematical Models

The storage states of gasses include (1) free gasses in fractures, (2) gas adsorbed on the surfaces of fractures, and (3) gas adsorbed within the matrix. During gas depletion, gas follows a sequential flow process: first, the free gas in the fractures is released, followed by the gas adsorbed on the fracture surfaces, and finally, the adsorbed gas within the matrix is released. The redistribution of gas pressure within the matrix facilitates the interaction of substances and stresses between the fracture and the matrix, causing matrix deformation to transition from local to global. When a fracture is filled with CO_2 gas, the free gas exerts pressure, generating local strain that increases the fracture aperture. Conversely, gas adsorbed on the surfaces of fractures and the matrix induces matrix expansion, resulting in a decrease in the fracture aperture. The mechanical mechanism of matrix expansion due to adsorption differs fundamentally from that caused by free gas [37].

A number of physical events occur within the matrix when gas is injected into coal: (1) Due to their high permeability, the gas pressure in fractures rapidly increases. Greater fracture expansion and matrix contraction occur in the parallel bedding direction because of the smaller Young's modulus and easier deformation, as shown in Figure 3a. This local behavior in the fractures converts the volume of fracture expansion into an equivalent volume of matrix contraction. (2) Pore strain is generated when gas molecules contact the fracture wall and spread into the matrix. As depicted in Figure 3b, more significant matrix expansion and fracture contraction occur in the parallel bedding plane direction. This local occurrence on the fracture surface results in the volume of fracture contraction being equal to the volume of matrix expansion. (3) The gas continues to diffuse within the matrix until a new equilibrium is established between the matrix and fractures. During this phase, global strain develops due to the localized increase in gas pressure. Both the matrix and the fractures expand as a result of this process, affecting the entire matrix region while the external forces remain constant. The expansion in the parallel bedding plane direction, featuring greater deformability, is more pronounced than that in the vertical bedding plane direction, as illustrated in Figure 3c.
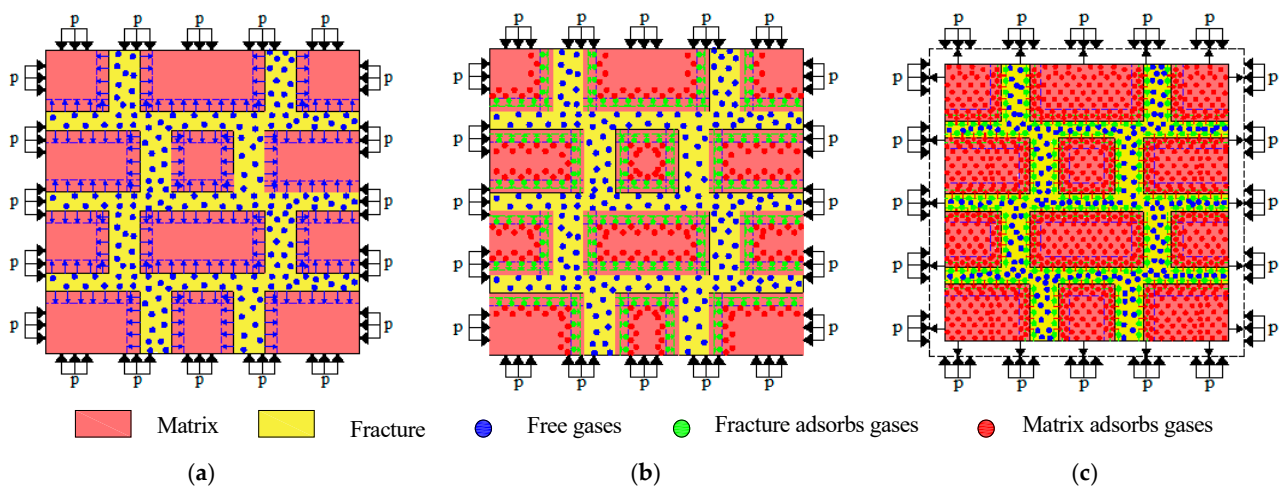
Figure 3. Conceptual model of coal–gas interactions. (**a**) The gas is injected into the coal. (**b**) The gas molecules come into contact with the fracture wall and diffuse into the matrix. (**c**) The gas reaches a new equilibrium between the matrix and the fracture.

The exposure of coal rock to adsorbed carbon dioxide gas results in the diffusion and adsorption of the gas, which causes internal expansion and overall deformation of the coal rock mass. This leads to a change in the degree of fracture opening. This fracture opening variation is usually described by the effective strain of the fracture, including the global strain and the local strain of the fracture [38]. The global strain represents the overall deformation of the coal, whereas the fracture local strain denotes the strain of the matrix block resulting from the uneven pressure between the fracture and the matrix [39]. During

the process of gas injection, the coal body experiences overall deformation and an increase in the size of the fracture. Concurrently, the local strain of the fracture initially widens the fracture opening and subsequently narrows it.

To replicate the gas adsorption behavior in coal and how the permeability evolves in three directions, a series of partial differential equations is established under the following assumptions [25,40]:

(1) The coal sample is characterized as a heterogeneous, linear elastic material exhibiting small strains;
(2) The system maintains isothermal conditions, with gas flowing through the coal pores being treated as an ideal gas, and the viscosity of the gas remains constant under these isothermal circumstances;
(3) The gas flow within the pores of coal adheres to Darcy's law.

2.1. Deformation Governing Equations

The control deformation relationship in the Navier type is as follows [30,41]:

$$Gu_{i,kk} + \frac{G}{1-2v}u_{k,ki} - \alpha p_{,i} - K\varepsilon_{s,i} + f_i = 0,\tag{1}$$

where G represents the shear modulus, u denotes displacement, v signifies Poisson's ratio, α indicates the Biot coefficient, p refers to the gas pressure in the pores, K represents the bulk modulus, and f represents the volume force. The directional components of the variables are indicated by the subscripts i and k, Einstein's summation convention is represented by the subscript kk, and the derivative of the variable is indicated by the subscript comma. In the above equation, the effects of pore pressure (the third term) and adsorption stress (the fourth term) are considered.

2.2. Governing Equations of Fluid Flow

The gas mass balance equation is defined as follows [42]:

$$\frac{\partial m}{\partial t} + \nabla \cdot (\rho_g \mathbf{q_g}) = Q_s,\tag{2}$$

where ρ_g denotes the gas density and where Q_s indicates the source of the gas. Both the free phase and the absorbed gas can be determined in the coal rock; therefore, the gas content m can be written as follows:

$$m = \rho_g \varphi + \rho_{ga}\rho_c \frac{V_L p_f}{p_f + p_L},\tag{3}$$

where the porosity is denoted by φ, the gas density under standard conditions by ρ_{ga}, the coal density by ρ_c, the Langmuir volume constant by V_L, the Langmuir pressure constant by p_L, and the gas pressure in the fracture system p_f.

Considering that gravity has a negligible and relatively minor influence [30], the Darcy velocity $\mathbf{q_g}$ can be obtained as [43]

$$\mathbf{q_g} = -\frac{k}{\mu}\nabla p_f,\tag{4}$$

where k represents the permeability and μ denotes the dynamic viscosity of the gas.

The diffusion equation is applied to describe the gas flow in the coal matrix, which can be written as follows [44]:

$$\nabla \cdot (D_{ke}\nabla C_{ke}) = \frac{\partial C_{ke}}{\partial t},\tag{5}$$

where C_{ke} denotes the concentration of the adsorbed gas, and D_{ke} represents the diffusion coefficient of the matrix. The gas concentration C_{ke} is determined in the Langmuir form,

$$C_{ke} = \frac{V_L p_m}{p_m + p_L},$$

(6)

where p_m denotes the gas pressure in the matrix system.

2.3. Permeability Equation

Since both global and local fracture strains influence coal fracture opening [40], the fracture opening equation can be expressed as follows:

$$\Delta b = \Delta b_v + \Delta b_{fl},$$

(7)

where Δb and Δb_v represent the changes in fracture opening due to the global strain of coal. The change in fracture opening resulting from local strain in the fracture zone is denoted by Δb_{fl}.

The following expression describes the change in fracture opening induced by local strain in the fracture zone [44],

$$\Delta b_{fl} = \frac{p_f - p_m}{K_f} b_0,$$

(8)

where K_f indicates the corrected fracture stiffness, where $K_f = a \, K_n$; a signifies the length of the matrix block [40]; K_n is the fracture stiffness; and b_0 represents the initial pore opening.

The change in fracture opening resulting from the global strain of the fracture is expressed as follows:

$$\Delta b_v = \varepsilon_v b_0,$$

(9)

where ε_v denotes the global strain and b_0 represents the initial pore opening.

The variation in fracture porosity is in accordance with the definition of fracture porosity [45],

$$\frac{\varphi_f}{\varphi_{f0}} = 1 + \frac{\Delta b}{b_0},$$

(10)

where ϕ_f represents the current fracture porosity and where ϕ_{f0} denotes the initial fracture porosity.

The experimental results indicate a relationship between fracture porosity and permeability, described as follows [46–48]:

$$\frac{k_f}{k_{f0}} = \left(\frac{\varphi_f}{\varphi_{f0}} \right)^3,$$

(11)

where k_f represents the current fracture permeability and where k_{f0} signifies the initial fracture permeability.

Considering that coal demonstrates both permeability anisotropy and mechanical characteristic heterogeneity [45], the fracture permeability can be represented as follows, where the permeability in each direction is influenced by the other two directions:

$$\begin{cases} \frac{k_{fx}}{k_{f0}} = 0.5 \left(\frac{\varphi_{fFac}}{\varphi_{f0}} \right)^3 + 0.5 \left(\frac{\varphi_{fBed}}{\varphi_{f0}} \right)^3 \\ \frac{k_{fy}}{k_{f0}} = 0.5 \left(\frac{\varphi_{fBut}}{\varphi_{f0}} \right)^3 + 0.5 \left(\frac{\varphi_{fBed}}{\varphi_{f0}} \right)^3 \\ \frac{k_{fz}}{k_{f0}} = 0.5 \left(\frac{\varphi_{fBut}}{\varphi_{f0}} \right)^3 + 0.5 \left(\frac{\varphi_{fFac}}{\varphi_{f0}} \right)^3 \end{cases}.$$

(12)

The fracture permeabilities of the vertical bedding planes, vertical face cleats, and vertical butt cleats are represented by the symbols k_{fx}, k_{fy}, and k_f, respectively. The fracture

porosities in the directions of butt cleats, face cleats, and bedding plane directions are denoted by ϕ_{fBut}, ϕ_{fFac}, and ϕ_{fBed}, respectively.

2.4. Coupling Process

Figure 2a comprehensively shows the multi-physical coupling process in CO_2 geological storage, covering the complex interaction of mechanics and fluid flow behavior between coal seam fractures and matrix systems. The coupling process is divided into three main parts as follows:

(1) Mechanical deformation of the coal seam

The fracture and matrix in coal seam deformation occur under the action of fluid pressure change and external stress, which is controlled by the deformation control equation. The degree of deformation depends on the mechanical parameters of the material, such as Young's modulus and Poisson's ratio, which affect the compressibility of the coal seam and its response to fluid pressure. The deformation of a coal seam directly affects the porosity and permeability of the fracture system and changes the gas flow path between the matrix and fracture. This coupling deformation leads to a dynamic change in the fracture system and ultimately changes the gas storage capacity and gas flow characteristics of the coal seam.

(2) Gas flow and transmission process

Gas flow in a fracture: Gas flow in a fracture system is described by Darcy's law, and its velocity is determined by the porosity, permeability, and fluid pressure gradient of the fracture. Fracture flow is affected by the dynamic change in fracture porosity, which in turn depends on the deformation to which the fracture is subjected (controlled by mechanical processes).

Gas flow in the matrix: the gas in the matrix is mainly diffused, and the gas desorbs from the adsorbed state (solid phase) to the free state (gas phase) and migrates to the fractures through the pores inside the matrix. This process is controlled by the diffusion coefficient and the Langmuir adsorption constant, which determines the equilibrium between gas adsorption and desorption. The flow in the matrix is also affected by the change in the fluid pressure field in the fracture system, and the matrix gas release is related to the fluid pressure gradient of the fracture and the matrix pore pressure difference.

(3) Coupling between fractures and the matrix

The fracture and matrix are coupled by a fluid pressure field. The change in fluid pressure leads to deformation of the fracture system, which in turn affects its permeability and flow capacity. Moreover, the decrease in pressure within the fracture triggers the desorption process of the gas in the matrix and drives the gas from the matrix into the fracture through diffusion. This coupling relationship forms a dynamic feedback loop. The alteration of fracture pressure results in the discharge of matrix gas, which in turn modifies the pressure within the fracture and its transmission path. This, in turn, influences the gas flow process of the entire coal seam.

The whole coupling process is centered on the deformation, fracture, and gas flow of the coal seam and involves complex interactions among multiple physical fields (mechanical fluid). The fracture system provides the main flow path of gas, and the matrix is the reservoir of gas. The two are coupled through fluid pressure and are constantly and dynamically adjusted. This model provides theoretical support for the study of CO_2 geological storage in coal seams and is helpful for optimizing the process of CO_2 geological storage.

3. Numerical Modeling

The coupled model was implemented and resolved with COMSOL Multiphysics (5.4a). By utilizing the finite element method, COMSOL Multiphysics supports all stages of simulation, encompassing geometry modeling, material parameter definitions, and physics

settings, culminating in solution and results processing by simulating single physics while enabling flexible coupling of various physics.

3.1. Geometry

Coal is a typical dual-porosity medium [49]. The mechanical properties of coal and the seepage of fluid in coal clearly exhibit anisotropy at the macroscopic level [36]. Fracture opening is determined using the permeability formula and the fracture opening formula (Equations (7)–(12)). The ambient temperature is not considered in the present model. The effects of Young's modulus, diffusion coefficient, Langmuir adsorption constant, and fracture and matrix geometric dimensions on the permeability were investigated, as illustrated in Figure 2c. In order to enhance alignment with laboratory testing and to ensure the model's accuracy and reliability, based on the theory of fluid–solid coupling (as shown in Figure 2a), a three-dimensional geometric model measuring 4.2 μm × 4.12 μm × 4.6 μm was created. The coal matrix consists of three dimensions: 1 μm × 1 μm × 1 μm, 1.5 μm × 1 μm × 1 μm, and 2 μm × 1 μm × 1 μm, with corresponding fracture widths of 0.2 μm, 0.1 μm, and 0.04 μm, respectively, as illustrated in Figure 2b.

3.2. Boundary Conditions and Parameter Selection

To ensure that the established model is highly consistent with the laboratory test process, the boundary conditions and initial values are set for the model with reference to the experimental conditions. The initial pressure of the coal block itself is 3 MPa; the six surfaces of the model injected with carbon dioxide only bear pressures increasing from 3 MPa to the maximum pressure of 4 MPa, and all six surfaces of the model are unconstrained.

To ensure the accuracy and convergence of the model, appropriate grid dissection was performed. Initially, the top xy-plane was meshed, and the fractures in the direction of the face cuttings were mapped. The number of distribution elements in the x direction was set to three, while the number of elements in the y direction that did not intersect with the end cuttings was eight, and the number of those that intersected with the end cuttings was two. Additionally, the fractures in the direction of the end cuttings were mapped, resulting in two distribution cells along the y direction and four distribution cells along the x direction, each side measuring 1 μm in length. The number of edge length distribution cells in the middle length of 1 μm was five, whereas two cells were designated for the middle length of 0.5 μm. The remaining matrix surface was subsequently mapped, and upon completion of the prior steps, the remaining section was swept, thereby finalizing the meshing of the entire model. The computational area consists of 18,720 mesh vertices, 16,530 hexahedra, 16,076 quadrilaterals, 4952 edge cells, 577 vertex cells, and 16,530 domain cells, yielding an average cell quality of 0.9777.

The values for the model's Young's modulus in the x, y, and z directions are 8662 MPa, 4430 MPa, and 15,419 MPa, respectively. The initial permeability values in the x, y, and z directions are 6.72×10^{-16} m^2, 6.71×10^{-16} m^2, and 9.60×10^{-18} m^2, respectively (where x indicates the direction of face cutting, y indicates the direction of end cutting, and z indicates the direction of vertical bedding). Equation (12) shows that the permeability in the x direction is the sum of half the permeability in the end-cutting direction and half the permeability in the vertical bedding direction. Furthermore, the Langmuir pressure constant is 3.5 MPa for all three directions, whereas the Langmuir adsorption constant is 0.1 in all three directions. The remaining parameters are detailed in Table 1 [25,30].

Table 1. Property parameters of the simulation model.

Symbol	Description	Value	Unit
v	Poisson's ratio	0.3	
ρ_c	The density of coal	1300	kg/m^3
α	Biot coefficient	0.67	
ρ_{ac}	CO_2 density under standard conditions	1.977	kg/m^3

Table 1. *Cont.*

Symbol	Description	Value	Unit
μ	Dynamic viscosity	1.84×10^{-5}	Pa·s
φ_0	Initial porosity	0.008	
V_L	Langmuir volume constant	0.015	m^3/kg
D	Diffusion coefficient	5×10^{-16}	m^2/s

3.3. Model Implementation

The model governs the deformation of coal through solid mechanics, the flow of CO_2 gas in fractures using Darcy's law, and the diffusion of CO_2 gas within the matrix via a general form of partial differential equation. The start time is set at 0, the stop time is set at $10^{3.5}$ s, and the step size is designated $10^{0.05}$ s, facilitating a strongly coupled solution for the three physical fields.

To prevent CO_2 leakage and control its risk more easily, step CO_2 injection is generally adopted at industrial sites [50]. This should be initiated with a low flow rate, and a pressure change should be observed. Thereafter, the injection volume should be increased in steps until the target volume is reached. Throughout this process, the injection pressure, flow, and temperature must be monitored in real time to avoid any potential coal seam rupture or CO_2 leakage. In our simulation, assuming that there is already 3 MPa of pressure in the coal seam, we simulate the process of increasing the CO_2 of the coal seam from 3 MPa to 4 MPa.

3.4. Fracture Opening

COMSOL Multiphysics was used to simulate the injection of 4 MPa of carbon dioxide to address the impact of coal sample adsorption on fracture opening and the permeability ratio k/k_0.

The gas contains numerous fractures, with local strain occurring because of the pressure difference between the fracture and the matrix, leading to an increase in fracture opening. The openings in the bedding planes, surface, and butt cleat directions increase rapidly, with the most significant changes observed in the parallel bedding direction and the smallest increase ratio noted in the face cleat direction, as illustrated in Figure 4a. The ratio of fracture opening to initial fracture opening in the parallel bedding plane is the highest, whereas the smallest ratio occurs in the butt cleat direction, as illustrated in Figure 4b. As gas molecules interact with the fracture wall and diffuse into the matrix, a decrease in fracture opening is observed in all three directions due to gas adsorption strain and pore strain. Once the gas pressure achieves a new equilibrium between subsystems, the fracture expands, resulting in an increase in fracture opening attributed to the global strain effect.
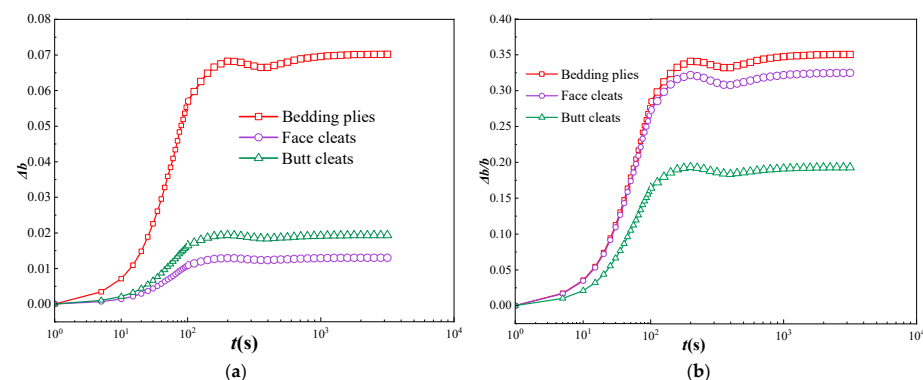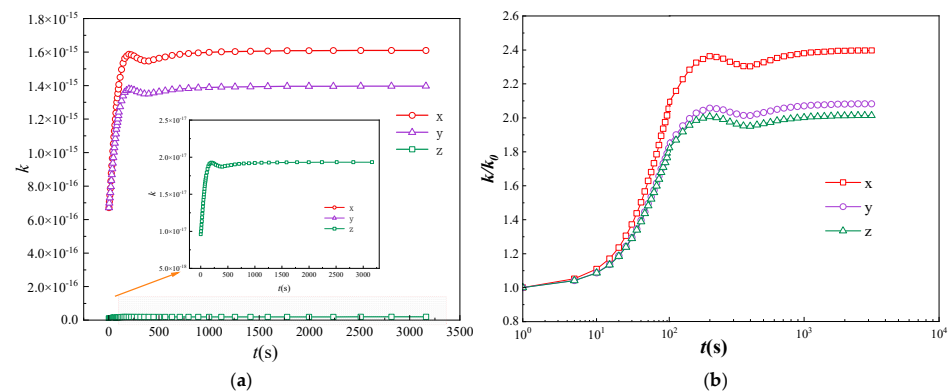

Figure 4. The relationship between fracture opening and time was simulated numerically. (**a**) Changes in the number of fracture openings and (**b**) the ratio of the change in fracture opening to the original fracture opening.

Fracture opening consistently exceeds the initial fracture opening throughout the entire process, from gas filling the fracture to a new equilibrium. Additionally, the changes in fracture opening are significantly greater in the bedding plane direction than in the cleavage direction.

3.5. Permeability k/k_0

The stratigraphic structure of the coal seam exhibits structural anisotropy, leading to a noticeable contrast in fracture openings when examined in parallel and perpendicular stratigraphic directions. This variation in fracture opening size subsequently affects the permeability of the coal seam, resulting in marked anisotropy.

The variation rules of permeability k and the ratio of permeability k/k_0 in different directions are depicted in Figure 5. As gas occupies the fracture, the fracture opening expands, leading to a corresponding increase in permeability k. The ratio of permeability k/k_0 also experiences a gradual increase. However, when gas molecules encounter the fracture wall and diffuse into the matrix, the gas adsorption strain and pore strain lead to a reduction in fracture opening. Consequently, this results in a decrease in both the permeability k and the permeability k/k_0. A new equilibrium in coal is achieved due to the global strain effect. Following this, the fracture opening gradually recovers and expands, as does the permeability k/k_0. Once equilibrium is attained between the matrix and the fracture, the fracture opening begins to recover and increase as a result of the global strain effect, leading to an increase in permeability (k) and a gradual restoration of permeability (k/k_0).

Figure 5. The relationship between the permeability k/k_0 and time was simulated numerically. (**a**) Changes in permeability. (**b**) The ratio of the change in permeability to the original permeability.

Throughout the entire process, from the initial gas filling of the fracture to the eventual establishment of a new equilibrium state, the permeability (k) in the x and y directions is relatively high, whereas the permeability in the z direction is the lowest. This is depicted in Figure 5a, which also demonstrates that the fracture openings in the laminar direction are larger and experience the most significant alterations. This observation is further supported by Figure 5b. During the process, from the initial filling of the fracture with gas to the attainment of a new equilibrium state, the ratio of permeability k/k_0 is found to be highest in the y direction and lowest in the z direction, as shown in Figure 5b. The permeability ratio k/k_0 consistently exceeds one in both directions, indicating that the injection of carbon dioxide gas improves the permeability of the coal body.

4. Results

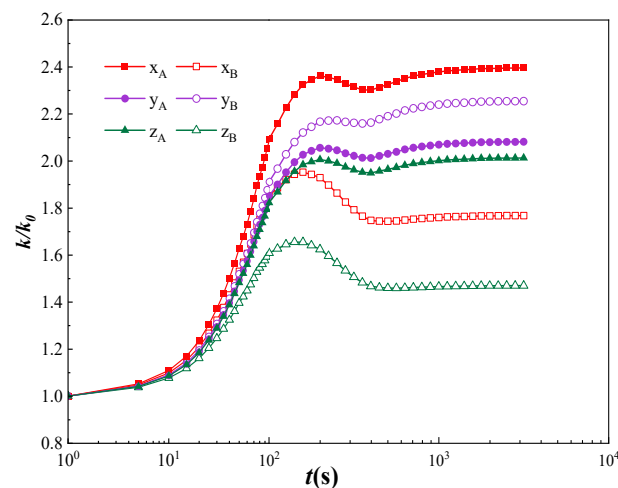### 4.1. Effect of Young's Modulus on Permeability

In accordance with the isotropic condition of Young's modulus, the relationships among the magnitudes of permeability k/k_0 are as follows: the largest ratio is determined in the y direction, the x direction, and the z direction. In the context of the anisotropy of Young's modulus, the relationships among the magnitudes of permeability k/k_0 are as

follows: x direction, y direction, and z direction. The letters x, y, and z in the figure retain their previously stated meanings, with the subscript "A" indicating anisotropic conditions and the subscript "B" indicating isotropic conditions.

Under the isotropic condition of Young's modulus, the permeability k/k_0 varies significantly among the three directions, whereas Young's modulus remains uniform across these directions. Additionally, the deformation is similarly influenced by the pore strain in all three directions. The anisotropy of deformation is governed primarily by the adsorption strain. Consequently, the difference in adsorption becomes the main factor contributing to permeability anisotropy. As adsorption increases, deformation also increases, resulting in decreased permeability. This is evident in the case of z-direction adsorption, which is stronger than the weaker adsorption in the y-direction. In the context of the anisotropic Young's modulus, the effects of both Young's modulus and the adsorption strain on deformation are clear. The permeability k/k_0 in the x direction is significantly greater than that in the y and z directions, whereas the permeability in the y and z directions is of comparable magnitude, as shown in Figure 6.

Figure 6. Effect of Young's modulus isotropy and anisotropy on the permeability k/k_0.

An increase in E_{ver}/E_{par} between vertical bedding planes and parallel bedding planes results in a corresponding increase in the permeability ratio (k/k_0) in the same direction. Furthermore, the curve becomes flatter, and the influences of the adsorption strain and pore strain of gas are less discernible. The variation in Young's modulus ratio between vertical bedding planes and parallel bedding planes has a more pronounced effect on the permeability than do the other factors.

The ratios of Young's modulus between the vertical and parallel laminae directions were 1:3, 1:5, and 1:7. The relationships among the permeabilities k/k_0 indicate that the permeability k/k_0 is greatest in the x direction, smaller in the y direction but comparable to that in the x direction, and significantly greater than that in the z direction. Additionally, the effects of pore strain and adsorptive strain exert substantial influences across all three directions. When the ratio of Young's modulus between the vertical and parallel laminae directions is 1:3, the permeability k/k_0 initially increases, then decreases, then increases again, and then reaches a plateau. Both the pore strain and adsorption strain significantly influence the permeability anisotropy. The ratio of Young's modulus between the vertical and parallel laminae directions was 1:5. The permeability of the k/k_0 image initially increases and then plateaus, with a slight decline in the y direction. The influence of the adsorption strain and pore strain is minimal, as illustrated in Figure 7. Among the three distinct ratios of Young's modulus, the permeability in the corresponding direction is the lowest when the ratio of Young's modulus in the perpendicular laminar direction to that in the parallel laminar direction is 1:3.
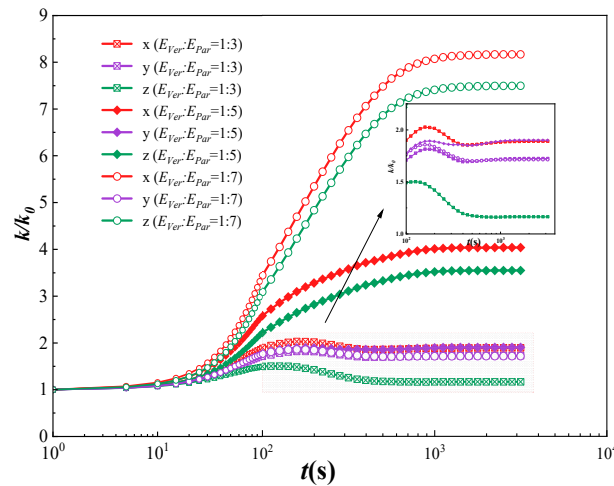
Figure 7. Effect of Young's modulus with different ratios of vertical bedding plane directions and parallel bedding plane directions on the permeability k/k_0.

4.2. Effect of the Diffusion Coefficient on the Permeability

The magnitude of the diffusion coefficient D does not affect the permeability relationship among the three directions. When the diffusion coefficient D is 5×10^{-14} m^2/s, 5×10^{-16} m^2/s, or 5×10^{-18} m^2/s, the permeability k/k_0 is much greater than that of the butt cleats and vertical bedding planes, and the butt cleats and vertical bedding planes are similar. When the diffusion coefficient $D = 5 \times 10^{-14}$ m^2/s and $D = 5 \times 10^{-16}$ m^2/s, the permeability k/k_0 is similar in the three directions, but when the diffusion coefficient $D = 5 \times 10^{-14}$ m^2/s, the peak value of the permeability k/k_0 is smaller, the gas adsorption strain and pore strain effects are not obvious, and the curve is relatively gentle, as displayed in Figure 8.
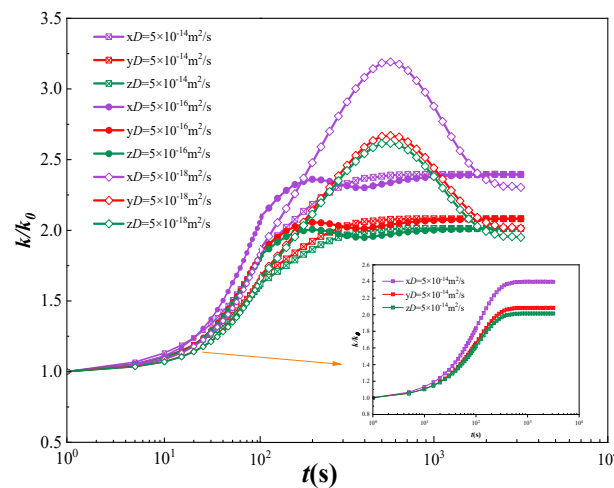
Figure 8. Effects of different diffusion coefficients D on the permeability k/k_0.

As the diffusion coefficient increases, the permeability peak (k/k_0) decreases, the curve becomes flatter, and the impact of gas adsorption behavior and pore strain becomes less pronounced. A higher diffusion coefficient (D) has little effect on the permeability peaks, whereas a decrease in D significantly impacts the permeability, as illustrated in Figure 8.

4.3. Effect of the Langmuir Adsorption Constant on the Permeability

The magnitude of the Langmuir adsorption constant does not influence the relationship between the permeability magnitude in the three directions, as shown in Figure 9. When $\varepsilon_L = 0.2$, the relationship of permeability k/k_0 is the same as that observed at 0.1. In

this scenario, the x direction has a significantly larger value than the y and z directions, which are comparable to each other. The relationship of permeability k/k_0 is clearly not pronounced across the three directions, indicating that the adsorption strain effect has a considerable effect on permeability anisotropy, especially in the x direction. An increase in the Langmuir adsorption constant results in a corresponding increase in the adsorption capacity. Conversely, overall expansion leads to a reduction in the local effect, which assumes a dominant role. Additionally, an increase in the peak permeability (k/k_0) leads to a reduction in the time required to reach a new equilibrium between the matrix and fractures. Nonetheless, as the curve flattens, the effects of the gas adsorption strain and pore strain become less significant. Additionally, both increases and decreases in the Langmuir adsorption constant significantly affect permeability, as depicted in Figure 9.
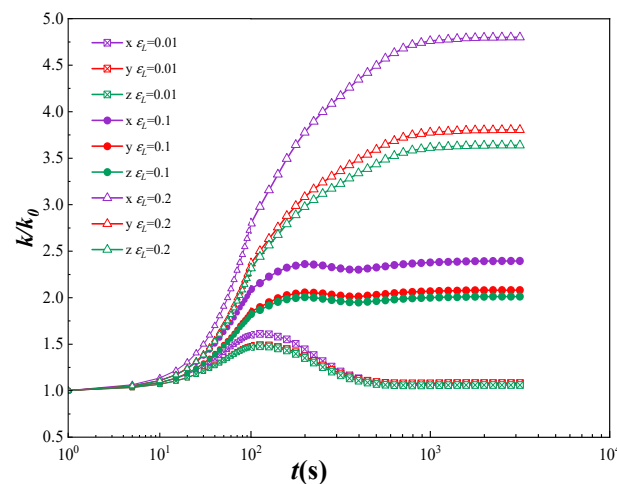

Figure 9. Effect of different Langmuir adsorption constants on the permeability k/k_0.

### 4.4. Effect of Fracture Size on Permeability in the Bedding Plane Direction

The size of the model bedding direction fracture width was changed so that it was 0.2 μm, 0.4 μm, or 0.6 μm, and the other conditions remained unchanged. The dimensions of the model bedding direction fracture width are altered to 0.2 μm, 0.4 μm, and 0.6 μm, with all other conditions remaining unaltered. The size of the fracture width in the bedding direction has no effect on the connection between k/k_0 and the size of the coal rock in the three directions. In all the cases, the values are greater in the x-direction than in the other directions, as illustrated in Figure 10. This phenomenon can be explained by the layered structure of the coal rock, where the fracture width in the bedding direction is greater than that in the cutting direction. As shown in Figure 10, a decrease in the fracture width in the bedding direction correlates with an increase in permeability (k/k_0) across all three directions. This trend is evident in the x, y, and z directions. The size of the fracture width in the bedding direction has the most significant effect on the permeability k/k_0 in the z direction, whereas it has the least impact in the y direction. For fracture widths of 0.4 and 0.6 μm in the bedding direction, the permeability k/k_0 in the z direction initially increases, then decreases, and subsequently increases again. The peak value of the second ascending stage is consistently lower than that of the first ascending stage, suggesting that the global strain is induced by gas diffusion. The equilibrium state in coal is achieved more quickly than that produced by gas molecules upon contact with the fracture wall and their diffusion into the matrix. Moreover, the strain and pore space strain resulting from gas adsorption and diffusion into the matrix are lower than those induced by gas adsorption and pore strain.
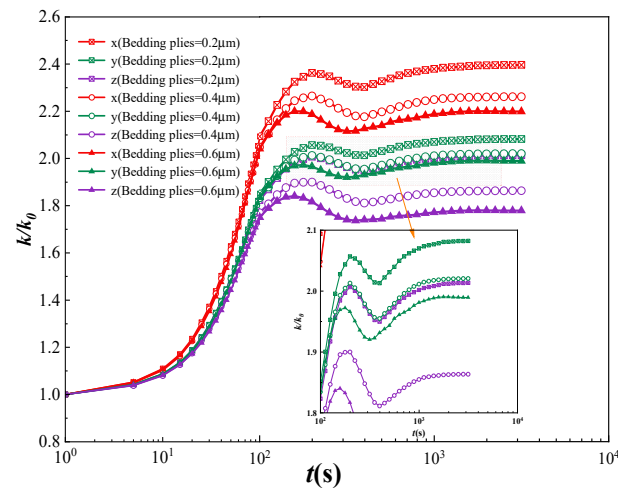
Figure 10. Effect of fracture size on the permeability k/k_0 along different bedding paths.

4.5. Effect of the Matrix Block Size on the Permeability

The dimensions of the model matrix block are adjusted to decrease its length, width, and height by 0.1 and 0.2 μm, respectively, while the other conditions remain unchanged. The size of the matrix block does not influence the permeability (k/k_0) in the three primary directions of the coal rock. As shown in Figure 11, this relationship results in higher permeability in the x direction than in the y direction and higher permeability in the y direction than in the z direction. With a decrease in the matrix block size, the relative width of the fracture increases, resulting in a corresponding increase in permeability (k_0). In contrast, the permeability (k/k_0) decreases. This trend is consistently noted across the x, y, and z directions. As the matrix block dimensions decrease, the descending stage of the image becomes less distinct, whereas the second ascending stage gains prominence. This results in a larger peak and a more uniform image, as depicted in Figure 11. This suggests that a decrease in the matrix block size leads to a reduction in the gas adsorption strain and pore strain after the interaction between the gas molecules and the fracture wall, facilitating diffusion into the matrix. Furthermore, the overall strain is generated by the gas diffusion process in the matrix until a new equilibrium is established, along with the time necessary to achieve this equilibrium.
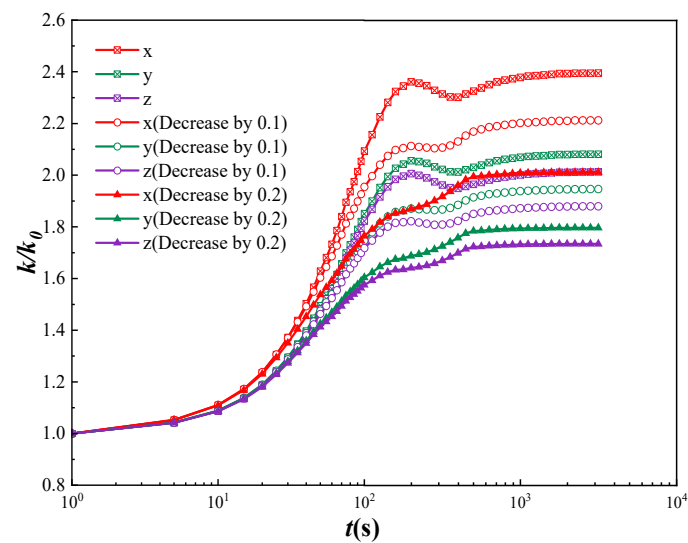
Figure 11. Effect of different matrix block sizes on the permeability k/k_0.

5. Discussion

5.1. Influence of Mechanical Properties

The bedding direction results in a larger fracture opening than the cleat direction does, resulting in greater gas storage, as illustrated in Figure 4. Consequently, the bedding direction serves as the primary space for industrial coal seam gas extraction and CO_2 storage. Under the influence of pore strain and adsorption strain, the permeability ratio (k/k_0) is more dependent on the variations in the direction of face cleats than on those in butt cleats. Additionally, the change in the direction of vertical bedding has a greater influence than that of horizontal bedding. This study offers theoretical support and recommendations for exploring methods to increase coal bed methane recovery and CO_2 storage, as demonstrated in Figure 5.

When $E_{ver}:E_{par}$ = 1:1, the permeability k/k_0 representation in the x and z directions can be categorized into three phases: an initial increase, a subsequent decrease, and a final stabilization. The permeability k/k_0 representation in the y direction can be segmented into four phases: an initial increase, a subsequent decrease, a subsequent recovery, and a final stabilization. The rebound phase is greater than the decrease phase. This phenomenon can be explained by the anisotropy of fracture opening, which is influenced mainly by the anisotropy of the adsorption strain. The key factor affecting permeability anisotropy is the variation in adsorption. Enhanced adsorption results in increased matrix deformation, leading to reduced fracture openings and, consequently, decreased permeability (k/k_0). When Young's modulus of a coal block exhibits anisotropy, the decreasing phase of the permeability k/k_0 representation in the x- and z-directions becomes less pronounced as the ratio of Young's modulus of the coal body between parallel bedding planes and vertical bedding planes increases. Moreover, the time taken to achieve equilibrium decreases progressively. When $E_{ver}:E_{par}$ = 1:3, the k/k_0 image of the x- and z-direction permeabilities initially increases, then decreases, and subsequently becomes flat. When $E_{ver}:E_{par}$ = 1:5 and $E_{ver}:E_{par}$ = 1:7, respectively. The k/k_0 image of the permeability in the x and z directions initially increases and then plateaus; the k/k_0 image of the permeability in the y direction initially increases, then decreases, and then plateaus. When $E_{ver}:E_{par}$ = 1:5 and $E_{ver}:E_{par}$ = 1:7, the x- and z-direction permeabilities initially increase and then reach a plateau. The images of permeability in the y direction reveal a pattern of initial increase, subsequent decrease, and eventual leveling off. However, the decline is less pronounced when $E_{ver}:E_{par}$ = 1:5. The anisotropy of Young's modulus affects the permeability anisotropy. The ratio of Young's modulus between the vertical and parallel stratigraphic directions is a critical factor affecting permeability, as shown in Figures 6 and 7. Adjusting this ratio has the potential to increase CBM recovery and improve CO_2 sequestration efficiency.

The maximum value of the rising stage, the minimum value of the falling stage, and the equilibrium value of the rebound stage of the permeability k/k_0 in the x direction increase with decreasing Young's modulus ratio. However, there is no falling stage when $E_{ver}:E_{par}$ = 1:5 and $E_{ver}:E_{par}$ = 1:7. When $E_{ver}:E_{par}$ = 1:3, the maximum and minimum values of permeability k/k_0 in the y and z directions are reached in the shortest time, and the minimum value of permeability k/k_0 in the z direction decreases with decreasing Young's modulus ratio. In the case of $E_{ver}:E_{par}$ = 1:5 and $E_{ver}:E_{par}$ = 1:7, a falling stage is observed. Conversely, no falling stage is evident in the case of $E_{ver}:E_{par}$ = 1:1 and $E_{ver}:E_{par}$ = 1:3. Additionally, no rebound stage is discernible for the z-direction permeability k/k_0. The three distinct Young's modulus ratios (k_{min}/k_{max}) are consistently less than 1, with the descending stage exhibiting a smaller magnitude than the ascending stage. When $E_{ver}:E_{par}$ = 1:5, k_{end}/k_{max} is greater than 1 in the x, y, and z directions, and the rebound stage is larger than the ascending stage. Additionally, the time required to reach the equilibrium value of the rebound stage is considerably longer than that required for other Young's modulus ratios. In Table 2, the equilibrium values are considerably larger than the final equilibrium values of the other Young's modulus ratios. Additionally, k_{end}/k_{max} is greater than 1.7 in both the x- and z-directions, the value in the rebound stage is greater than that in the upward stage, and the minimum value in the downward stage is similar to the equilibrium value in the rebound

stage. The time required to reach the maximum value of the rising stage in the x and z directions is less than that in the y direction, and the time required to reach the minimum value of the falling stage in the x and y directions is less than that in the z direction, as illustrated in Table 2.

Table 2. Effect of different Young's moduli of coal on the permeability k/k_0.

Name		Increase		Descend		Rebound		Descend/Increase k_{min}/k_{max}	Rebound/Increase k_{end}/k_{max}
		$(k/k_0)_{max}$	Time(s)	$(k/k_0)_{min}$	Time(s)	$(k/k_0)_{end}$	Time(s)		
$E_{ver}{:}E_{par}=1{:}1$	x	1.95	158	1.74	398	1.76	1000	0.89	0.90
	y	2.17	199	2.16	354	2.24	1000	1.00	1.03
	z	1.67	158	1.46	501	-		0.87	-
$E_{ver}{:}E_{par}=1{:}3$	x	2.02	158	1.85	398	1.88	1000	0.92	0.93
	y	1.81	178	1.69	398	1.71	794	0.93	0.94
	z	1.50	126	1.17	562	-		0.78	-
$E_{ver}{:}E_{par}=1{:}5$	x	3.09	158	-		4.03	1585	-	1.30
	y	1.89	178	1.58	446	1.90	1412	0.84	1.01
	z	2.64	158	-		3.54	1412	-	1.34
$E_{ver}{:}E_{par}=1{:}7$	x	4.70	158	-		8.17	1995	-	1.74
	y	1.86	158	1.70	501	1.71	794	0.91	0.92
	z	4.23	158	-		7.50	1995	-	1.77

5.2. Influence of Mobility Performance

The diffusion coefficient D has a significant effect on the time needed for a new equilibrium state. An increase in D does not significantly impact the peak value of permeability k/k_0, whereas a decrease in D has a more significant effect on permeability, as illustrated in Figure 8. When $D = 5 \times 10^{-14}$ m^2/s, the permeability k/k_0 representation initially increases and then plateaus. When $D = 5 \times 10^{-16}$ m^2/s, the permeability k/k_0 representation first increases, then decreases, subsequently recovers, and finally stabilizes, with the magnitude of the rebound phase being comparable to that of the falling phase, although the duration of the rising phase is longer. When $D = 5 \times 10^{-18}$ m^2/s, the permeability k/k_0 represents an initial increase followed by a decrease and then a leveling off, with both the rising and falling phases being clearly evident, as illustrated in Figure 8.

The required times for the extreme values (maximum value, minimum value, and equilibrium value) in the three directions are almost the same under the same diffusion coefficient. It can also be determined that as the diffusion coefficient decreases, the required time increases. As the diffusion coefficient increases, the maximum value of the permeability k/k_0 rising stage in the x, y, and z directions decreases. Conversely, as the diffusion coefficient decreases, the maximum value of the permeability k/k_0 rising stage in the aforementioned directions increases. This is demonstrated in the cases of $D = 5 \times 10^{-16}$ m^2/s and $D = 5 \times 10^{-18}$ m^2/s, which correspond to the three permeability directions. The minimum value of the k/k_0 descending stage is similar, but the time needed to reach the minimum value when $D = 5 \times 10^{-16}$ m^2/s is observed to be much smaller than that needed when $D = 5 \times 10^{-18}$ m^2/s. The equilibrium values of k/k_0 in the rebound stage corresponding to the permeability in three directions when $D = 5 \times 10^{-14}$ m^2/s and $D = 5 \times 10^{-16}$ m^2/s are similar. However, the time required to reach equilibrium when $D = 5 \times 10^{-16}$ m^2/s is significantly shorter than that required when $D = 5 \times 10^{-18}$ m^2/s. The time required to reach equilibrium is markedly shorter than that required at $D = 5 \times 10^{-18}$ m^2/s, and there is no falling stage at $D = 5 \times 10^{-14}$ m^2/s and no rebound stage at $D = 5 \times 10^{-18}$ m^2/s, as illustrated in Table 3. When $D = 5 \times 10^{-16}$ m^2/s in the x, y, and z directions, the ratio of the minimum to maximum values of k is approximately 0.97. When $D = 5 \times 10^{-18}$ m^2/s in the x, y, and z directions, the ratio of the minimum to maximum values of k is approximately 0.75. The descending stage is smaller than the ascending stage (as shown in Table 3). When $D = 5 \times 10^{-14}$ m^2/s in the x, y, and z directions, the ratio of the maximum to minimum values of k is approximately 1. In the x, y, and z directions, the rebound stage is slightly larger than the upward stage (as in Table 3). This is evidenced by the value of 0.8 in the x, y, and z directions and the value of k_{end}/k_{max}, which is approximately 1. As the value of D

increases, the downward stage becomes less pronounced. Conversely, as *D* decreases, the maximum value of the upward stage can be obtained, the minimum value of the downward stage can be reached, and the equilibrium value of the rebound stage can be attained more slowly. In industrial applications, the diffusion coefficient can be optimized by adjusting the temperature and pressure of the system to increase coal bed methane extraction and CO_2 storage efficiency.

Table 3. Effects of different diffusion coefficients on the permeability k/k_0.

Name		Increase		Descend		Rebound		Descend/Increase k_{min}/k_{max}	Rebound/Increase k_{end}/k_{max}
		$(k/k_0)_{max}$	Time(s)	$(k/k_0)_{min}$	Time(s)	$(k/k_0)_{end}$	Time(s)		
$D = 5 \times 10^{-14}$ m²/s	x	2.14	199	-		2.40	794	-	1.12
	y	1.92	199	-		2.08	794	-	1.08
	z	1.86	199	-		2.01	794	-	1.08
$D = 5 \times 10^{-16}$ m²/s	x	2.36	199	2.30	398	2.39	1258	0.97	1.01
	y	2.06	199	2.01	398	2.08	1258	0.98	1.01
	z	2.01	199	1.95	398	2.01	1258	0.97	1.00
$D = 5 \times 10^{-18}$ m²/s	x	3.19	562	2.31	2511	-		0.72	-
	y	2.67	562	2.02	2511	-		0.76	-
	z	2.62	562	1.96	2511	-		0.75	-

5.3. Influence of Adsorption Properties

When $\varepsilon_L = 0.01$, the permeability k/k_0 representation initially increases, then decreases, and subsequently levels off, with the changes in the rising and falling phases being similar. When $\varepsilon_L = 0.1$, the permeability k/k_0 representation first increases, then decreases, subsequently recovers, and finally stabilizes, with the magnitude of the rebound phase being comparable to that of the falling phase. When $\varepsilon_L = 0.2$, the permeability k/k_0 representation initially increases and then plateaus, as shown in Figure 9.

The maximum value of the rising stage, the minimum value of the falling stage, and the equilibrium value of the rebound stage of the permeability k/k_0 in the x, y, and z directions increase with increasing Langmuir adsorption constant. Furthermore, the time required for the permeability k/k_0 to reach the maximum value of the rising stage at $\varepsilon_L = 0.01$ is less than the time required at $\varepsilon_L = 0.1$ and $\varepsilon_L = 0.2$. Furthermore, the time required for the permeability k/k_0 to reach the minimum value of the falling stage decreases with increasing Langmuir adsorption constant. Notably, there is no descending stage at $\varepsilon_L = 0.2$. In contrast, the time required for the permeability k/k_0 to reach the equilibrium value of the rebound stage increases with increasing Langmuir adsorption constant. Additionally, there is no rebound stage at $\varepsilon_L = 0.01$, as illustrated in Table 4. The minimum and maximum values of *k* are about 0.7 and 0.97, respectively, in the x, y, and z directions when $\varepsilon_L = 0.01$ and about 0.7 and 0.97, respectively, in the x, y, and z directions when $\varepsilon_L = 0.1$. The falling stage is smaller than the rising stage (as shown in Table 4). The k_{end}/k_{max} is approximately in the x, y, and z directions and is approximately 1 when $\varepsilon_L = 0.1$ and approximately 1 in the same directions when $\varepsilon_L = 0.2$. In the latter case, the rebound stage is slightly larger than the rise stage (see Table 4). As the Langmuir adsorption constant increases, the maximum value of the rising phase and the minimum value of the falling phase also increase, whereas the time required to achieve equilibrium decreases. In industrial applications, the Langmuir adsorption constant can be optimized by adjusting the system temperature to increase the benefits of coal bed methane recovery and CO_2 storage.

Table 4. Effects of different Langmuir adsorption constants on the permeability k/k_0.

Name		Increase		Descend		Rebound		Descend/Increase k_{min}/k_{max}	Rebound/Increase k_{end}/k_{max}
		$(k/k_0)_{max}$	Time(s)	$(k/k_0)_{min}$	Time(s)	$(k/k_0)_{end}$	Time(s)		
$\varepsilon_L = 0.01$	x	1.61	112	1.07	749	-		0.66	-
	y	1.49	112	1.08	891	-		0.72	-
	z	1.48	112	1.06	707	-		0.72	-

Table 4. *Cont.*

Name		Increase		Descend		Rebound		Descend/Increase k_{min}/k_{max}	Rebound/Increase k_{end}/k_{max}
		$(k/k_0)_{max}$	Time(s)	$(k/k_0)_{min}$	Time(s)	$(k/k_0)_{end}$	Time(s)		
$\varepsilon_L = 0.1$	x	2.36	200	2.30	398	2.39	1258	0.97	1.01
	y	2.06	200	2.01	398	2.08	1258	0.98	1.01
	z	2.01	200	1.95	398	2.01	1258	0.97	1.00
$\varepsilon_L = 0.2$	x	3.78	200	-		4.80	1778	-	1.27
	y	3.08	200	-		3.80	1413	-	1.23
	z	2.98	200	-		3.63	1413	-	1.22

5.4. Influence of Geometric Modeling

When the fracture size in the bedding direction is 0.2 µm, 0.4 µm, and 0.6 µm, the permeability k/k_0 representation initially increases, followed by a subsequent decrease and subsequent recovery, and finally levels off. The rebounding stage demonstrates a magnitude of change comparable to that determined during the falling stage, as displayed in Figure 10.

As the fracture size increases, the permeability k/k_0 in all three directions decreases. In the rising stage, the maximum value is reached, whereas in the falling stage, the minimum value is observed. In the rebound stage, the equilibrium value is attained. A smaller fracture width in the bedding direction corresponds to a higher permeability k/k_0. Furthermore, the time required for different fracture sizes to reach the maximum value (or equilibrium value) is dependent on the direction of the fracture. The k_{min}/k_{max} ratio is about 0.97, whereas the k_{end}/k_{max} ratio is about 1 in all directions for varying fracture sizes. The equilibrium value of the rebound stage is comparable to the maximum value of the rise stage, as illustrated in Table 5.

Table 5. Effects of different fracture sizes on the permeability k/k_0.

Fracture Size in Bedding Direction		Increase		Descend		Rebound		Descend/Increase k_{min}/k_{max}	Rebound/Increase k_{end}/k_{max}
		$(k/k_0)_{max}$	Time(s)	$(k/k_0)_{min}$	Time(s)	$(k/k_0)_{end}$	Time(s)		
0.2 µm	x	2.36	200	2.30	398	2.39	1258	0.97	1.01
	y	2.06	200	2.01	398	2.08	1258	0.98	1.01
	z	2.01	200	1.95	398	2.01	1258	0.97	1.00
0.4 µm	x	2.27	200	2.18	398	2.26	1778	0.96	1.00
	y	2.01	200	1.96	355	2.02	1584	0.98	1.00
	z	1.90	200	1.81	398	1.86	1778	0.95	0.98
0.6 µm	x	2.20	158	2.11	316	2.20	1778	0.96	1.00
	y	1.97	178	1.92	316	1.99	1584	0.97	1.01
	z	1.84	158	1.73	354	1.80	1584	0.94	0.98

When the length, width, and height of the matrix block are reduced by 0.1 µm while remaining unchanged, the permeability k/k_0 representation initially increases, then decreases, subsequently recovers, and finally levels off. With a 0.1 µm reduction in dimensions, the descending stage is not prominent, whereas the second ascending stage is more pronounced. When the length, width, and height of the matrix block are reduced by 0.2 µm, the permeability k/k_0 first increases, then continues to rise, and subsequently tends to decrease. The rebound stages are observed, with no falling stage present. A smaller matrix block size correlates with a larger fracture width, resulting in an increased permeability k_0 and a decreased permeability k/k_0, as shown in Figure 11.

The maximum value of the rising stage, the minimum value of the falling stage, and the equilibrium value of the rebound stage of the permeability k/k_0 in the x, y, and z directions decrease with decreasing matrix block size. Furthermore, the time required to reach the maximum value (or the equilibrium value) becomes shorter. In addition, there is no falling stage when the size of the matrix block decreases by 0.2 µm, as illustrated in Table 6. The reduction in the matrix block size leads to a smaller gas adsorption strain and pore strain upon contact between gas molecules and the fracture wall and diffusion into the matrix.

The greater the global strain resulting from the gas diffusion process is, the shorter the time required to achieve equilibrium. When the matrix block size remains constant, k_{min}/k_{max} is approximately 0.97 and k_{end}/k_{max} is approximately 1 in all directions. When the matrix block size is decreased by 0.1 µm, k_{min}/k_{max} is approximately 1 and k_{end}/k_{max} is approximately 1.04 in all directions. When the matrix block size is decreased by 0.2 µm, k_{end}/k_{max} is greater than or equal to 1. Table 6 shows that as the matrix block size decreases, the minimum value of the descending stage increases and becomes less pronounced. Additionally, the rebound stage equilibrium value surpasses the maximum value of the ascending stage.

Table 6. Effects of different matrix sizes on the permeability k/k_0.

Matrix Block Size		Increase		Descend		Rebound		Descend/Increase k_{min}/k_{max}	Rebound/Increase k_{end}/k_{max}
		$(k/k_0)_{max}$	Time(s)	$(k/k_0)_{min}$	Time(s)	$(k/k_0)_{end}$	Time(s)		
Decrease by 0 µm	x	2.36	200	2.30	398	2.39	1258	0.97	1.01
	y	2.06	200	2.01	398	2.08	1258	0.98	1.01
	z	2.01	200	1.95	398	2.01	1258	0.97	1.00
Decrease by 0.1 µm	x	2.11	200	2.10	281	2.21	1258	1.00	1.05
	y	1.87	200	1.86	281	1.94	1258	0.99	1.04
	z	1.82	200	1.81	281	1.88	1258	0.99	1.03
Decrease by 0.2 µm	x	1.82	125	-		2.00	501	-	1.10
	y	1.65	125	-		1.99	501	-	1.21
	z	1.61	125	-		1.72	501	-	1.07

(Note: A decrease of 0 µm means no change in the matrix size (the same as that shown in Figure 3b)).

5.5. Comparison with Existing Permeability Models

Most of the previous models used the dual or single porosity model to describe the evolution behavior of permeability anisotropy [25,29,30,32,33]. In these types of models, the influence of the fracture matrix on the permeability anisotropy is not considered or is not implicitly described.

Zhu Wancheng et al. [51] extended the dual-porosity model to consider the damage of gas adsorption and dissolution on coal seams, incorporating the expansion and contraction of coal as well as the destruction of coal caused by gas adsorption and desorption. This was performed on the basis of the principle of damage mechanics. The strain in the vicinity of the fracture wall is defined as the local strain of the fracture, whereas the strain of the coal body is defined as the overall strain. The matrix permeability and fracture permeability models essentially reflect the influence of both the local strain and the overall strain on the permeability of the matrix and fracture, as well as the expansion/shrinkage and damage of the coal caused by gas adsorption/desorption. Considering the interrelationship between fracture porosity and effective strain within a fracture, the fracture permeability model is derived in accordance with the cubic law.

$$\frac{k_f}{k_{f0}} = [1 + \frac{1}{\varphi_{f0}}(\Delta \varepsilon v + \frac{p_f - p_m}{K_m} - \Delta \varepsilon_{fs})]^3,$$ (13)

where k_{f0} is the initial fracture permeability, k_f is the current fracture permeability, ϕ_{f0} is the initial fracture porosity, ε_v is the overall strain, K_m is the bulk modulus of the coal matrix, and ε_{fs} is the gas adsorption-induced strain of the fracture.

Guo Haijun et al. [52] simplified the coal matrix and fissure into geometric shapes with regular shapes when they carried out relevant theoretical research. Specifically, the scaling features of the simplified geometry are considered to be equivalent fracture widths and equivalent matrix scales. A new permeability evolution model (ECDP model) based on the structural equivalence characteristics of double-porosity coal is established. The ECDP model takes into account the effects of the dual pore structure, effective stress,

and adsorption deformation of the coal matrix on coal permeability. The quantitative relationship between coal permeability and equivalent scale characteristics is as follows:

$$k = \frac{a^2 \varphi_f^3}{162} \text{ or } k = \frac{b^2 \varphi_f}{18},$$ (14)

where *a* is the equivalent matrix side length of coal, *b* is the equivalent fracture side length, and ϕ_f is the fracture porosity.

This treatment ignores the effects of the microstructure of the matrix and fractures and the deformation heterogeneity caused by the adsorption and diffusion of gasses in the matrix. In this work, an explicit modeling method is employed to provide an accurate description of the microstructure of the fracture matrix, and the influence of mechanical parameter anisotropy on permeability evolution is investigated. This constitutes a valuable contribution and enhancement to the preceding work.

5.6. Limitations and Future Work

In this work, the influence of fracture and matrix mechanical anisotropy on permeability anisotropy is examined through numerical simulation and theoretical modeling methods. The evolution of permeability is investigated, which is crucial for the comprehensive development of coal bed methane energy and the geological storage of carbon dioxide. However, the research has focused primarily on numerical analysis, and certain deficiencies remain that require improvement and supplementation in future studies. Consequently, the following suggestions and prospects are proposed:

(1) This paper emphasizes numerical simulations and theoretical analysis, which could be enhanced by incorporating raw coal tests to further investigate the anisotropy laws and increase confidence in the findings.

(2) The temperature of coal seams at various depths is a variable that affects the diffusion coefficient and Langmuir adsorption constant. Controlling the temperature can optimize the benefits of industrial pumping and sequestration. The impact of temperature has not been incorporated into this model. In theory, an increase in temperature results in a greater velocity of gas molecules and a shorter time to reach equilibrium. To increase the model precision, it would be beneficial to integrate a temperature field into the model, thereby facilitating an investigation into the influence of temperature on the gas seepage process.

(3) The size of the matrix block and fracture, which directly affects the gas flow path and gas storage capacity, is very important in modeling. Fracture size affects permeability, whereas matrix size affects the gas release speed. In this work, one size is selected for modeling because it conforms to the actual permeability theory of coal–rock fracture, which may not be the most consistent with the actual experiment. Therefore, the sizes of the matrix blocks and fractures in the model can be further optimized and explored.

(4) The number of matrix blocks and fractures employed during modeling is relatively limited. However, the number of model matrix blocks and fractures can be increased to achieve a greater degree of fidelity in the simulation results for coal–rock fracture permeability, thereby approximating the actual results more closely.

(5) This model can be verified via laboratory tests. The coal sample to be tested is selected, and the coal sample is preferably square. The permeability was tested via a special 3D-printed rubber sleeve with a triaxial percolation system [53,54]. The strain gauge should be attached to the coal sample above and below, around and before. The coal block is put into the penetration instrument to ensure that both ends of the sample are sealed. Constant air pressure is applied to one end to measure the volume of gas flowing through the coal sample and the passage time. The permeability can be calculated using Darcy's law or related formulas according to the gas flow and the geometric size of the sample. The model is verified by the strain condition and permeability change in the coal block, and the model is further optimized.

(6) The traditional dual or single porosity model is frequently employed to elucidate the permeability evolution law observed in laboratory settings [23,24,27,36,55,56] and to construct a multitude of permeability anisotropy models [25,29,30,32,33]. Nevertheless, this approach is inadequate for accounting for the impact of fractures and the matrix on the anisotropic evolution of permeability. This paper proposes a micro discrete model that fully considers the influence of structural and mechanical anisotropy on permeability anisotropy. The work in this paper can be a good supplement to the double pore medium model. It can be obtained in the following way: through many experiments or numerical simulations (the method in this paper). The universal law of the influence of the matrix and fracture structure and mechanical anisotropy is obtained. The implicit equation is used to express it, which is integrated into the traditional double-pore medium model.

(7) This paper proposes a micro discrete model that considers the influence of structural and mechanical anisotropy on permeability anisotropy in a comprehensive manner. (i) Nevertheless, for large-scale industrial applications, this work is severely limited by the inability to accurately characterize the microstructure of the matrix and fracture at the field scale [57]. (ii) Even if feasible, it would necessitate the expenditure of a considerable amount of computational and time resources. The objective is to upgrade the rules obtained from the conceptual model to the REV scale, obtain general universal rules, and establish a permeability anisotropy model based on the double-pore medium model. A geometric model is constructed using finite element software, such as COMSOL Multiphysics (5.4a), to represent the heterogeneous fracture–matrix properties (permeability and Young's modulus) at an industrial scale. The permeability anisotropy model is then applied to the computational node. In this way, the microscopic model presented in this paper is applied to the field.

6. Conclusions

In light of the intricate coal rock deformation and gas flow characteristics associated with the gas adsorption process in coal and rock, the impact of heterogeneous carbon dioxide gas adsorption on the permeability k/k_0 of these materials is modeled using COMSOL Multiphysics software. The main findings are as follows:

(1) Throughout the process of gas filling the fracture to achieve a new equilibrium state in the coal, the fracture opening and permeability k/k_0 initially increase, followed by a decrease and then another increase. The variation in fracture opening in the bedding ply direction is significantly greater than that in the face cleat direction, exceeding that in the butt cleat direction. Moreover, the permeability k/k_0 in the face cleat direction remains considerably greater than that in both the butt cleats and vertical bedding ply directions, consistently exceeding the initial value.

(2) When Young's modulus is isotropic, the permeability k/k_0 is the highest in the butt cleats direction, and when Young's modulus is anisotropic, the permeability k/k_0 is the highest in the face cleats direction. Increases and decreases in Young's modulus ratio in the vertical and parallel bedding directions significantly affect the permeability.

(3) The gas diffusion behavior and the Langmuir adsorption constant in the matrix do not influence the permeability relationship across the three directions. An increase in the diffusion coefficient results in a reduction in the peak value of permeability k/k_0 and a smoother curve. Conversely, a decrease in D significantly impacts permeability. A higher Langmuir adsorption parameter is correlated with a larger peak value of permeability k/k_0 and a smoother curve. Both increases and decreases in the Langmuir adsorption constant distinctly affect permeability.

(4) The size of the fracture in the bedding direction and the dimensions of the matrix block influence the permeability relationship across the three directions. An increase in fracture size leads to a decrease in the peak value of permeability k/k_0, whereas changes in fracture size do not alter the shape of the permeability k/k_0 profile. A reduction in the matrix block size results in a lower permeability k/k_0, less pronounced

descending stages of the profile, more evident ascending stages in the latter part, a larger peak value, and a smoother profile.

Data Availability Statement: The raw data supporting the conclusions of this article will be made available by the authors on request.

References

1. Chen, L. Environmental cost of sustainable development and climate change: Can SAARC shift some liability with renewable energy and efficiency? *Environ. Sci. Pollut. Res.* **2021**, *28*, 67137–67149. [CrossRef] [PubMed]
2. Fragkos, P.; van Soest, H.L.; Schaeffer, R.; Reedman, L.; Köberle, A.C.; Macaluso, N.; Evangelopoulou, S.; De Vita, A.; Sha, F.; Qimin, C. Energy system transitions and low-carbon pathways in Australia, Brazil, Canada, China, EU-28, India, Indonesia, Japan, Republic of Korea, Russia and the United States. *Energy* **2021**, *216*, 119385. [CrossRef]
3. Rogelj, J.; Popp, A.; Calvin, K.V.; Luderer, G.; Emmerling, J.; Gernaat, D.; Fujimori, S.; Strefler, J.; Hasegawa, T.; Marangoni, G. Scenarios towards limiting global mean temperature increase below 1.5 C. *Nat. Clim. Change* **2018**, *8*, 325–332. [CrossRef]
4. Shuxun, S. Research review on technical effectiveness of CO_2 geological storage and enhanced coalbed methane recovery. *Coal Geol. Explor.* **2018**, *46*, 1–9.
5. Garnier, C.; Finqueneisel, G.; Zimny, T.; Pokryszka, Z.; Lafortune, S.; Défossez, P.; Gaucher, E.C. Selection of coals of different maturities for CO_2 Storage by modelling of CH_4 and CO_2 adsorption isotherms. *Int. J. Coal Geol.* **2011**, *87*, 80–86. [CrossRef]
6. Liu, S.; Liu, T.; Zheng, S.; Wang, R.; Sang, S. Evaluation of carbon dioxide geological sequestration potential in coal mining area. *Int. J. Greenh. Gas Control* **2023**, *122*, 103814. [CrossRef]
7. White, C.M.; Strazisar, B.R.; Granite, E.J.; Hoffman, J.S.; Pennline, H.W. Separation and capture of CO_2 from large stationary sources and sequestration in geological formations—Coalbeds and deep saline aquifers. *J. Air Waste Manage. Assoc.* **2003**, *53*, 645–715. [CrossRef]
8. Chen, D.; Pan, Z.; Liu, J.; Connell, L.D. Characteristic of anisotropic coal permeability and its impact on optimal design of multi-lateral well for coalbed methane production. *J. Pet. Sci. Eng* **2012**, *88*, 13–28. [CrossRef]
9. Pan, Z.; Connell, L.D. Modelling permeability for coal reservoirs: A review of analytical models and testing data. *Int. J. Coal Geol.* **2012**, *92*, 1–44. [CrossRef]
10. Pan, Z.; Ye, J.; Zhou, F.; Tan, Y.; Connell, L.D.; Fan, J. CO_2 storage in coal to enhance coalbed methane recovery: A review of field experiments in China. *Coal Geol. China* **2017**, *60*, 754–776.
11. Gu, F.; Chalaturnyk, R. Permeability and porosity models considering anisotropy and discontinuity of coalbeds and application in coupled simulation. *J. Pet. Sci. Eng.* **2010**, *74*, 113–131. [CrossRef]
12. Lu, G.; Wei, C.; Wang, J.; Zhang, J.; Quan, F.; Tamehe, L.S. Variation of surface free energy in the process of methane adsorption in the nanopores of tectonically deformed coals: A case study of middle-rank tectonically deformed coals in the Huaibei Coalfield. *Energy Fuels* **2019**, *33*, 7155–7165. [CrossRef]
13. Lu, J.; Yin, G.; Deng, B.; Zhang, W.; Li, M.; Chai, X.; Liu, C.; Liu, Y. Permeability characteristics of layered composite coal-rock under true triaxial stress conditions. *J. Nat. Gas Sci. Eng.* **2019**, *66*, 60–76. [CrossRef]
14. Barenblatt, G.; Zheltov, Y.P.; Kochina, I. Basic concepts in the theory of seepage of homogeneous liquids in fissured rocks. *J. Appl. Math. Mech.* **1960**, *24*, 852–864. [CrossRef]
15. Xia, K.; Wang, M.; Fu, Y.; Wu, B.; Xu, Y.; Yao, W. Advances in dynamic test of deep rocks considering in-situ mechanical and hydraulic conditions. *Deep Resour. Eng.* **2024**, *1*, 100020. [CrossRef]
16. Okubo, S.; Fukui, K.; Qingxin, Q. Uniaxial compression and tension tests of anthracite and loading rate dependence of peak strength. *Int. J. Coal Geol.* **2006**, *68*, 196–204. [CrossRef]
17. Li, Y.-W.; Zhang, J.; Liu, Y. Effects of loading direction on failure load test results for Brazilian tests on coal rock. *Rock Mech. Rock Eng.* **2016**, *49*, 2173–2180. [CrossRef]
18. Zhao, Y.; Zhao, G.-F.; Jiang, Y.; Elsworth, D.; Huang, Y. Effects of bedding on the dynamic indirect tensile strength of coal: Laboratory experiments and numerical simulation. *Int. J. Coal Geol.* **2014**, *132*, 81–93. [CrossRef]
19. Zhao, Y.; Gong, S.; Zhang, C.; Zhang, Z.; Jiang, Y. Fractal characteristics of crack propagation in coal under impact loading. *Fractals* **2018**, *26*, 1840014. [CrossRef]
20. Pomeroy, C.; Robinson, D.J. The effect of applied stresses on the permeability of a middle rank coal to water. In *International Journal of Rock Mechanics and Mining Sciences & Geomechanics Abstracts*; Elsevier: Amsterdam, The Netherlands, 1967.

21. Koenig, R.; Stubbs, P. Interference testing of a coalbed methane reservoir. In Proceedings of the SPE Unconventional Resources Conference/Gas Technology Symposium, Louisville, Kentucky, 18–21 May 1986; SPE: Houston, TX, USA, 1986.

22. Gash, B.W.; Volz, R.F.; Potter, G.; Corgan, J.M. The effects of cleat orientation and confining pressure on cleat porosity, permeability and relative permeability in coal. In Proceedings of the SPWLA/SCA Symposium, Oklahoma City, OK, USA, 14–17 June 1992.

23. Liu, Z.; Liu, D.; Cai, Y.; Pan, Z. Experimental study of the effective stress coefficient for coal anisotropic permeability. *Energy* **2020**, *34*, 5856–5867. [CrossRef]

24. Yan, Z.; Wang, K.; Zang, J.; Wang, C.; Liu, A. Anisotropic coal permeability and its stress sensitivity. *Int. J. Min. Sci. Technol.* **2019**, *29*, 507–511. [CrossRef]

25. Zhang, H.; Liu, J.; Elsworth, D. How sorption-induced matrix deformation affects gas flow in coal seams: A new FE model. *Int. J. Rock Mech. Min. Sci.* **2008**, *45*, 1226–1236. [CrossRef]

26. Yang, D.; Qi, X.; Chen, W.; Wang, S.; Dai, F. Numerical investigation on the coupled gas-solid behavior of coal using an improved anisotropic permeability model. *J. Nat. Gas Sci. Eng.* **2016**, *34*, 226–235. [CrossRef]

27. Wang, K.; Zang, J.; Wang, G.; Zhou, A. Anisotropic permeability evolution of coal with effective stress variation and gas sorption: Model development and analysis. *Int. J. Coal Geol.* **2014**, *130*, 53–65. [CrossRef]

28. Wang, H.; Marongiu-Porcu, M. A unified model of matrix permeability in shale gas formations. In Proceedings of the SPE Reservoir Simulation Conference, Houston, TX, USA, 23–25 February 2015; SPE: Houston, TX, USA, 2015.

29. Wang, G.; Massarotto, P.; Rudolph, V. An improved permeability model of coal for coalbed methane recovery and CO_2 geosequestration. *Int. J. Coal Geol.* **2009**, *77*, 127–136. [CrossRef]

30. Peng, Y.; Liu, J.; Wei, M.; Pan, Z.; Connell, L.D. Why coal permeability changes under free swellings: New insights. *Int. J. Coal Geol.* **2014**, *133*, 35–46. [CrossRef]

31. Pan, Z.; Ma, Y.; Danesh, N.N.; Connell, L.D.; Sander, R.; Down, D.I.; Camilleri, M. Measurement of shale anisotropic permeability and its impact on shale gas production. In Proceedings of the SPE Asia Pacific Unconventional Resources Conference and Exhibition, Brisbane, Australia, 9–11 November 2015; SPE: Houston, TX, USA, 2015.

32. Liu, J.; Chen, Z.; Elsworth, D.; Miao, X.; Mao, X. Evaluation of stress-controlled coal swelling processes. *Int. J. Coal Geol.* **2010**, *83*, 446–455. [CrossRef]

33. Liu, H.-H.; Rutqvist, J. A new coal-permeability model: Internal swelling stress and fracture–matrix interaction. *Transp Porous Media* **2010**, *82*, 157–171. [CrossRef]

34. Zhou, H.; Rong, T.; Wang, L.; Mou, R.; Ren, W. A new anisotropic coal permeability model under the influence of stress, gas sorption and temperature: Development and verification. *Int. J. Rock Mech. Min. Sci.* **2020**, *132*, 104407. [CrossRef]

35. Li, J.; Li, B. Modeling of anisotropic coal permeability under the effects of matrix-fracture interaction. *J. Nat. Gas Sci. Eng.* **2021**, *93*, 104022. [CrossRef]

36. Tan, Y.; Pan, Z.; Liu, J.; Kang, J.; Zhou, F.; Connell, L.D.; Yang, Y. Experimental study of impact of anisotropy and heterogeneity on gas flow in coal. Part I: Diffusion and adsorption. *Fuel* **2018**, *232*, 444–453. [CrossRef]

37. Cui, G.; Liu, J.; Wei, M.; Shi, R.; Elsworth, D. Why shale permeability changes under variable effective stresses: New insights. *Fuel* **2018**, *213*, 55–71. [CrossRef]

38. Karacan, C.Ö. Swelling-induced volumetric strains internal to a stressed coal associated with CO_2 sorption. *Int. J. Coal Geol.* **2007**, *72*, 209–220. [CrossRef]

39. Cui, G.; Xia-Ting, F.; Pan, Z.; Chen, T.; Liu, J.; Elsworth, D.; Tan, Y.; Wang, C. Impact of shale matrix mechanical interactions on gas transport during production. *J. Pet. Sci. Eng* **2019**, *184*, 106524. [CrossRef]

40. Biot, M.A. General theory of three-dimensional consolidation. *J. Appl. Phys.* **1941**, *12*, 155–164. [CrossRef]

41. Detournay, E.; Cheng, A.H.-D. Fundamentals of poroelasticity. In *Analysis and Design Methods*; Elsevier: Amsterdam, The Netherlands, 1993; pp. 113–171.

42. Cheng, W.; Cui, G.; Tan, Y.; Elsworth, D.; Wang, C.; Yang, C.; Chen, T.; Jiang, C. A multi-layer nanocased model to explain the U-shaped evolution of shale gas permeability at constant confining pressure. *Fuel* **2024**, *359*, 130478. [CrossRef]

43. Shao, J.-F.; Yu, Z.; Liu, Z.; Vu, M.-N.; Armand, G. Numerical analysis of thermo-hydromechanical process related to deep geological radioactive repository. *Deep Resour. Eng.* **2024**, *1*, 100001. [CrossRef]

44. Cui, G.; Liu, J.; Wei, M.; Feng, X.; Elsworth, D. Evolution of permeability during the process of shale gas extraction. *J. Nat. Gas Sci. Eng.* **2018**, *49*, 94–109. [CrossRef]

45. Wu, Y.; Liu, J.; Elsworth, D. Development of permeability anisotropy during coalbed methane production. In Proceedings of the ARMA US Rock Mechanics/Geomechanics Symposium, Salt Lake, UT, USA, 27–30 June 2010; ARMA: Alexandria, UA, USA, 2010.

46. Cui, X.; Bustin, R.M.J.A.B. Volumetric strain associated with methane desorption and its impact on coalbed gas production from deep coal seams. *AAPG Bull.* **2005**, *89*, 1181–1202. [CrossRef]

47. Liu, J.; Chen, Z.; Elsworth, D.; Qu, H.; Chen, D. Interactions of multiple processes during CBM extraction: A critical review. *Int. J. Coal Geol.* **2011**, *87*, 175–189. [CrossRef]

48. Liu, J.; Elsworth, D.; Brady, B. Linking stress-dependent effective porosity and hydraulic conductivity fields to RMR. *Int. J. Rock Mech. Min. Sci.* **1999**, *36*, 581–596. [CrossRef]

49. Jiang, C.; Zhao, Z.; Zhang, X.; Liu, J.; Elsworth, D.; Cui, G. Controlling effects of differential swelling index on evolution of coal permeability. *J. Rock Mech. Geotech. Eng.* **2020**, *12*, 461–472. [CrossRef]

50. Sun, Z.; Elsworth, D.; Cui, G.; Li, Y.; Zhu, A.; Chen, T. Impacts of rate of change in effective stress and inertial effects on fault slip behavior: New insights into injection-induced earthquakes. *J. Geophys. Res. Solid Earth* **2024**, *129*, e2023JB027126. [CrossRef]
51. Zhu, W.; Liu, L.; Liu, J.; Wei, C.; Peng, Y. Impact of gas adsorption-induced coal damage on the evolution of coal permeability. *Int. J. Rock Mech. Min. Sci.* **2018**, *101*, 89–97. [CrossRef]
52. Guo, H.; Wang, K.; Cheng, Y.; Yuan, L.; Xu, C. Model development and analysis of coal permeability based on the equivalent characteristics of dual-porosity structure. *J. Geophys. Eng.* **2020**, *17*, 313–327. [CrossRef]
53. Tan, Y.; Pan, Z.; Liu, J.; Wu, Y.; Haque, A.; Connell, L.D. Experimental study of permeability and its anisotropy for shale fracture supported with proppant. *J. Nat. Gas Sci. Eng.* **2017**, *44*, 250–264. [CrossRef]
54. Tan, Y.; Pan, Z.; Liu, J.; Feng, X.-T.; Connell, L.D. Laboratory study of proppant on shale fracture permeability and compressibility. *Fuel* **2018**, *222*, 83–97. [CrossRef]
55. Pan, Z.; Connell, L.D. Modelling of anisotropic coal swelling and its impact on permeability behaviour for primary and enhanced coalbed methane recovery. *Int. J. Coal Geol.* **2011**, *85*, 257–267. [CrossRef]
56. Lou, Z.; Wang, K.; Zang, J.; Zhao, W.; Qin, B.; Kan, T. Effects of permeability anisotropy on coal mine methane drainage performance. *Eng. Fract. Mech.* **2021**, *86*, 103733. [CrossRef]
57. Chen, J.; Dai, Z. Metaheuristic algorithms for groundwater model parameter inversion: Advances and prospects. *Deep Resour. Eng.* **2024**, *1*, 100009. [CrossRef]